HLPW-4/GMGW-3: High Order Discretization Technology Focus Group Workshop Summary

Marshall C. Galbraith[*]
Massachusetts Institute of Technology, Cambridge, MA, 02139

Steve L. Karman[†]
Oak Ridge National Laboratory, 1 Bethel Valley Road, Oak Ridge, TN, 37831

This paper summarizes the High-Order Technical Focus Group (HO-TFG) submissions for the joint 4th AIAA High Lift Prediction(HLPW-4) and 3rd Geometry and Mesh Generation Workshop (GMGW-3). The goal of the workshop was to assess the state-of-the-art in mesh generation and computational fluid dynamics software. The Common Research Model High-Lift (CRM-HL) variant served as the primary focus of the workshop, and a 2D airfoil section from the CRM-HL was used as a verification test case. The HO-TFG was tasked with generating high-order curved meshes for both geometries, and computing high-order solutions using both Reynolds Averaged Navier-Stokes and scale resolving formulations. While limited by computational resources, the final results demonstrate the potential of higher-order methods to increase solution accuracy with a lower degree of freedom count relative to second-order discretizations.

I. Nomenclature

D = Cartesian dimensions (two- or three-dimensional)
DOF = degrees of freedom
N = number of Degrees of Freedom
P = solution polynomial degree
Q = mesh polynomial degree
Re = Reynolds number
h = characteristic length scale $h = N^{-1/D}$

---

[*] Research Engineer, Department of Aeronautics and Astronautics, AIAA Senior Member

[†] Modeling and Simulation Engineer, Computational Sciences and Engineering Division, AIAA Associate Fellow

AIAA Aviation 2022 Forum, June 2022, Chicago, IL, AIAA Paper 2022-3292

II. Introduction

The 4th High Lift Prediction Workshop (HLPW-4) [1] was held in conjunction with the 3rd Geometry and Mesh Generation Workshop (GMGW-3) [2] in January 2022 at the AIAA SciTech Conference in San Diego, California. The HLPW series [3–5] seeks to advance the state-of-the-art in predicting the high-lift flows using Computational Fluid Dynamics (CFD) software through cooperation/collaboration in the international community. Hence, all data, generated by both the organizers and participants is publicly available. Similarly, the GMGW series [6, 7] of workshops seeks to improve performance, accuracy, and applicability in geometry and mesh generation software for aerospace applications, and to provide documentation of best practices for both geometry and mesh generation.

The primary focus of the HLPW-4/GMGW-3 joint effort is the high-lift Common Research Model (CRM-HL) [8, 9]. This geometry is publicly available and is a major component of coordinated wind tunnel testing for the purpose of validating and improving CFD technology. In addition, a cross sectional airfoil cut of the CRM-HL, referred to as 2D CRM-HL here, is used to verify workshop participants' implementation of the Spalart-Allmaras (SA) turbulence model [10].

Unlike previous AIAA prediction workshops where participants worked individually and all results were compared at the workshop event, the HLPW-4/GMGW-3 was organized into Technology Focus Groups (TFG) where groups of active participants and observers collaborated, and a summary of those collaborations were presented at the workshop by the TFG leads. The six TFGs are:

1) Geometry Modeling and Preparation for Meshing (GEOM)
2) Fixed Grid Reynold's Averaged Navier-Stokes (RANS)
3) Mesh Adaptation for RANS (ADAPT)
4) High Order Discretization (HO)
5) Hybrid RANS/Large Eddy Simulation (HRLES)
6) Wall-Modeled LES (WMLES) and Lattice-Boltzmann (WMLESLB)

This paper provides a summary specifically for the HO-TFG. Summaries from the other TFG leads are available in Refs. [11–15] and an overall summary of the HLPW-4/GMGW-3 effort is provided in Ref. [16]

There were two major challenges for the HO-TFG: first, simply generating high-order curved meshes with the geometric complexities of the CRM-HL, and second, obtaining high-order solutions. The authors are not aware of any high-order Finite Element Method (FEM) solutions on geometry of this complexity in the literature. Hence, the HO-TFG sought to answer the following key questions:

1) Can 3D curved meshes be generated for the CRM-HL?
2) What mesh quality metrics are used to evaluate high order meshes?
3) How well do the curved meshes conform to the actual geometry?
4) Can high-order FEM/Finite Volume (FV) schemes be used with the CRM-HL configuration?

5) What are the y^+ normal distance requirement for LES/WMLES with high-order finite element schemes?

The first three questions are addressed in Section IV, and the last two in Sections VII and VIII. The remainder of the paper also includes a discussion of the nomenclature used by the HO-TFG in Section III, details about the difficulties with generating high-order curved meshes and the successfully generated meshes in Section IV, information about the CFD solutions submitted by the HO-TFG members in Section V, the results from the 2D CRM-HL verification case in Section VI, a DOF convergence study for the 3D CRM-HL in Section VII, and finally the results from an angle of attack sweep in Section VIII.

III. High-Order TFG Nomenclature

Finite element methods use polynomial expansions to approximate the solution for a partial differential equation (PDE) within a mesh element, as well as to represent the geometric shape of an element. Numerous different symbols are used throughout the high-order methods literature to represent the solution and mesh polynomial degrees. In order to facilitate discussion and clear communication, the HO-TFG adopted the notation of P for solution polynomial degree, and Q for mesh polynomial degree. A Q1 mesh uses linear interpolation to represent an element, which is consistent with classical finite volume and finite difference schemes. A higher-order Q2 mesh uses a quadratic polynomial representation of the element with additional modes in the element. This is accomplished by adding additional vertices on the edges of the element that provide support for high-order Lagrangian basis functions. The higher-order polynomial representation allows the element to “curve” and hence better represent curved geometry.

The L^2-error for a polynomial solution of degree P is expected to decay at a rate of h^{P+1} with mesh refinement. Hence, a P1 solution representation in a finite element scheme is 2nd-order accurate, P2 is 3rd-order accurate and so forth. Notably, if both the primal and adjoint solutions of an elliptic problem are sufficiently smooth, the error in an output functional, such as lift, decays at a rate of h^{2P} [17] (h^{2P+1} for hyperbolic problems [18]). For a finite volume discretization, the P notation refers to the degree of the polynomial reconstruction scheme. Again, the order of accuracy is expected to be h^{P+1}.

IV. Curved Finite Element CFD Mesh Generation

A. Meshing Guidelines

The workshop organizing committee prepared a set of mesh-generation guidelines for construction of CRM-HL meshes based on experience from previous workshops with fixed-grid RANS solvers. These general guidelines included specification of desired minimum spacing at viscous walls, clustering to pertinent geometric features, and a schedule of expected mesh growth factors. These guidelines would result in a family of meshes with a specific increase in size that could be used for a grid convergence study of the CFD solutions. The organizing committee supplied several mesh families with different grid topologies including all tetrahedral, prism-tetrahedral, and hexahedral-tetrahedral. Sizes ranged from 22 million cells and 12 million nodes for the “A” Hex-Tet mesh to 1.2 billion and 203 million nodes for the “D” Tet mesh.

The HO-TFG required high-order finite element meshes for the CRM-HL which have curved sides and an increased number of degrees of freedom within each element. These types of meshes are typically created by starting with a linear mesh, adding additional vertices along edges and internal to each element to achieve the desired polynomial degree (mesh Q-degree), and then smoothing the mesh to improve element quality. The workshop committee supplied meshes, following the general mesh-generation guidelines, resulted in a family of linear meshes that are too large to be practical for the high-order mesh elevation and curving process. Many of the HO-TFG were performing analysis on limited computer resources and were not able to use the supplied linear meshes. So, a supplemental set of mesh generation guidelines for the HO-TFG was created that extended the mesh family in the coarser direction using the same growth factor strategy. Three additional levels were created in the HO Meshing Guidelines Supplement, AA, AAA, and AAAA (coarsest). The y^+ requested spacing values reported in the general meshing guidelines and the HO Supplement were calculated using the Pointwise® flat plate y^+ calculator.

An initial set of coarse linear meshes, starting with the AAAA parameter set, was generated using Pointwise®. Linear meshes were elevated to quadratic order. However, participants were still unable to use the meshes on their respective computer systems. So, a new family of coarse, medium, fine and extra-fine linear meshes were created using Pointwise®. These linear meshes were supplied to HO-TFG participants. Pointwise® and Barcelona Super Computing elevated these meshes to quadratic order. INRIA used a separate mesh generation process to generate linear and quadratic meshes for CRM-HL.

B. Geometry Findings/Lessons Learned

Generating linear meshes for the HO-TFG encountered the same issues as those reported by the general workshop committee. The most troublesome spot were the pinch points where the wing meets the wing under slat surface, shown in Fig. 1. The geometry definition was corrected to ensure the curves approaching the pinch point were indeed tangent and did not cross. However, the mesh curving process assumes a quadratic polynomial and attempts to represent the curve more accurately than using linear straight sides. Unfortunately, there is no guarantee that the quadratic mesh does not cross. This could happen if the geometry curve was higher order than quadratic. This is depicted in Fig. 2 where the mesh curve and geometry curve approach the horizontal line. The order of the geometry curve is unknown during the meshing operation. The mesh curve is positioning the interior point in the middle of the curve. It is possible this produces a quadratic shape that crosses the horizontal line. Here, this issues is resolved by moving the endpoint of the mesh edges at the pinch point to a location close to where the mesh crosses over, as shown in the Fig. 2c. This will

---

https://www.Pointwise.com/yplus/

increase the angle in the corner and will change the quadratic representation to eliminate the crossover of the two mesh curves.

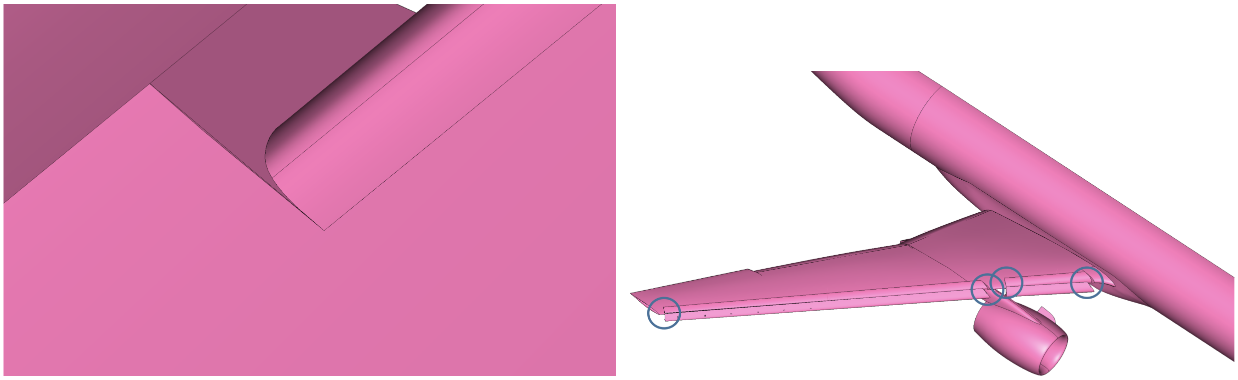

(a) Wing slat cutout where the wing under slat surface intersect the outboard wing section.

(b) Similar pinch points occur at several locations along the wing leading edge.

Fig. 1 Geometric pinch points

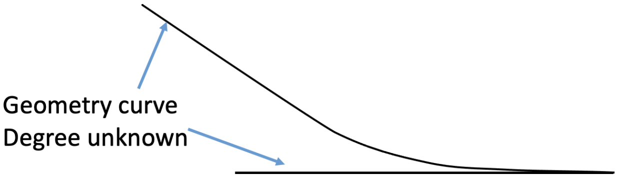

(a) Spline Curves

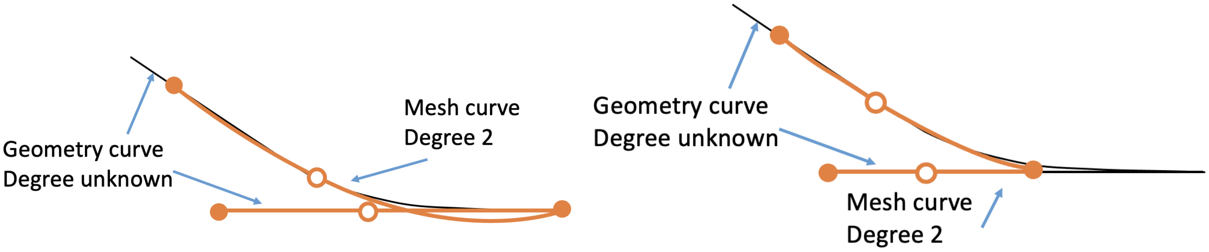

(b) Intersecting Q2 mesh curves (high-order hollow vertex)

(c) Resolved Q2 mesh curves

Fig. 2 Invalid curved mesh on a geometric pinch point

C. High Order Meshes Generated

Table 1 lists the HO-TFG participants that contributed meshes to the workshop. Three groups submitted quadratic meshes for the CRM-HL configuration. Pointwise® provided linear meshes in the Coarse, Medium, Fine, and Extra-Fine sequences using the Pointwise®, Pointwise® Inc., commercial meshing software. Pointwise® then used a research code, HP-Curvemesh[19], to create quadratic meshes. Many participants of the HO-TFG were attempting WM-LES solutions. Several additional meshes were created by Pointwise® to meet specific needs for these solver applications. Barcelona

---

https://www.pointwise.com

Super Computing started with the Pointwise® linear CRM-HL meshes and used their software ParCur [20–22] to generate quadratic meshes. INRIA used their software, ho-feflo.a, to create quadratic CRM-HL meshes.

Two additional configurations were meshed by the HO-TFG participants. The 3D NASA Juncture Flow Model (JFM) was provided as a meshing test case to exercise the mesh curving software. No flow solutions were attempted. Pointwise® generated a full sequence of Q2 meshes. GridPro also provided 3D JFM high order meshes, these being the structured hexahedral variety. In addition, GridPro generated 2D quadratic meshes for a flow solver calibration case, the 2D cut of the HL-CRM airfoil cross section. High order CRM-HL meshes have been made available to the public, posted to the HLPW website [23].

In addition to the submitted grids, a family of expertly crafted 2D CRM-HL Q1 meshes generated by the systematic mesh generation studies in Ref. [24] (referred to as the Turbulence Modelling Resource (TMR) meshes here) were also used for the verification case.

Table 1 High-Order TFG Grid Generation Submissions

Submission	Primary Organization	Meshing Tools	Contribution
H-001	Cadence/ORNL	Pointwise®, HP_CurveMesh	CRM-HL (Q2)
H-003	GridPro	GridPro	2D CRM-HL (Q2)
H-006	INRIA	ho-feflo.a	CRM-HL (Q2)
H-019	Barcelona Sup. Cent.	Pointwise®, ParCur	CRM-HL (Q2)

D. Shape Conformity

The use of high order meshes should result in more accurate geometry representation in the mesh. To demonstrate the improved accuracy a shape conformity metric was calculated and compared for several of the generated meshes. A detailed definition of shape conformity is provided in the HO-TFG section of the workshop webpage [1] in the High Order Mesh Metrics document.

Linear elements have planar triangular faces (or non-planar quadrilateral faces). Curved meshes improve the representation of the surface with increasing accuracy depending on the degree of the mesh. The shape conformity metric measures how well the discrete curved surface matches the underlying geometry. It is defined as the integration of the difference between the mesh surface and the geometry surface over the surface triangular or quadrilateral element. Shape conformity is defined as the average distance between the mesh and the surface. The shape conformity metric is computed over each surface element. This metric produces a dimensional quantity in the units of the mesh length scale. For planar surfaces all mesh orders should produce machine zero values, indicating the mesh is on the planar surface.

---

https://www.gridpro.com

For curved boundaries the linear mesh should exhibit the largest error. Increasing the mesh order should produce smaller error values.

Table 2 shows the shape conformity for the medium mesh. The maximum error and the average error are shown for three body components in the mesh for linear and quadratic versions of the mesh. Note, the surface mesh contains the same surface elements. One has linear shaped triangles and the other has quadratic triangles. The table shows a dramatic reduction in error from the linear to quadratic. Barcelona Super Computing performed the same calculation on their mesh for the entire vehicle, shown in Table 3. They include a cubic Q3 mesh in the result. The errors in the cubic mesh show an additional improvement in the geometry representation.

Table 2 H-001: Medium mesh. Selected body components. $y^+ \approx 1$

	Max. Error		Avg. Error	
Body	Q1	Q2	Q1	Q2
Fuselage	1.27	0.21	0.11	2.6×10^{-3}
Nacelle	0.37	4.9×10^{-2}	0.023	4.6×10^{-4}
Wing	0.26	3.6×10^{-2}	5.7×10^{-3}	1.9×10^{-4}

Table 3 H-019: Medium mesh. Full vehicle. $y^+ \approx 100$

	Max. Error			Avg. Error		
Body	Q1	Q2	Q3	Q1	Q2	Q3
Full Vehicle	1.48	0.25	0.12	0.1	9.8×10^{-4}	2.9×10^{-4}

V. High-Order CFD Solution Submissions

The list of CFD solution submissions for the HO-TFG is shown in Table 4. Two organizations participated in the HO-TFG as well as other TFGs. However, participants were asked not to submit the same data to multiple TFGs. Hence, the Massachusetts Institute of Technology (MIT) group submitted the A-013 data set to the ADAPT-TFG and to the HO-TFG as H-004; both are included in this summary for comparison purposes. In addition, the University of Kansas group participated in the HO-TFG as well as WMLESLB-TFG and chose to submit their data to the latter TGF as W-047. Participants solved either the steady/unsteady RANS equations with the SA turbulence model (RANS-SA), or scale resolving LES equations.

The MIT submissions H-004/A-013 uses the SANS [25, 26] CFD solver with a Continuous Galerkin Variational Multiscale with Discontinuous subscales (VMSD) [27, 28] discretization used to solve the steady RANS-SA equations.

The steady solutions are obtained via quasi-Newton Pseudo Time Continuation (PTC) implicit scheme with machine zero residuals. Results were submitted for the 2D CRM-HL using a-priori Q1 meshes provided on the TMR website, Q1 and Q2 meshes provided by GridPro, as well as adapted meshes generated using the Mesh Optimization via Sampling and Synthesis (MOESS) adaptation algorithm [29, 30]. The MOESS algorithm seeks the optimal mesh given a maximum DOF constraint that minimizes the error estimate in an output functional; drag is used as the output functional in both submissions. The A-013 only includes second order accurate P1 results with linear Q1 meshes, whereas H-004 includes high-order P2 solutions and Q2/Q3 meshes. SANS is not isoparametric, hence, some submissions have different Q and P values. More in-depth analysis of these submissions are available in Refs. [31, 32].

The H-005 submission used the United States Department of Defense High Performance Computing Modernization Program (HPCMP) Computational Research and Engineering Acquisition Tools and Environments CREATE$^{\text{TM}}$-AV Kestrel component COFFE [33] CFD solver to solve the steady RANS-SA equations for the 2D CRM-HL airfoil with a Continuous Galerkin Streamline Upwing Petrov Galerkin (SUPG) discretization. A PTC implicit scheme is used to achieve machine zero residuals for the steady RANS equations. Both second order P1 and higher order P2 solutions are submitted using TMR and GridPro meshes. COFFE is isoparametric; hence P and Q values are always the same.

The Nextflow_ITW [34] CFD solver used in submission H-012 has a k-exact (FV) reconstruction scheme along with a special grid pre-processing tool HO_DualMaker to take advantage of high-order meshes in the context of a FV discretization. An explicit time marching scheme is used to solve the RANS-SA equations. Results for both 2D and 3D CRM-HL calculations were submitted, and more details about the submissions are available in Ref. [35].

The Boeing company was not an active participant in the HO-TFG, and primarily participated in the ADAPT-TFG. However, the H-023 submission is a single high-order P2 solution using the Boeing General Geometry Navier-Stokes (GGNS-T1) [36, 37] solver for the 3D CRM-HL. GGNS uses an isoparametric Continuous Galerkin SUGP discretization and a PTC scheme to obtain machine zero residuals.

The H-013 submission uses the maDG [38] CFD solver, which uses a high-order Discontinuous Galerkin discretization to solve the scale-resolving Implicit LES (ILES) equations for the 3D CRM-HL. The submission includes high-order P1 through P3 solutions, but is currently limited to only using Q1 meshes. An implicit BDF2 with ILU-GMRES time marching scheme is used to advance the solution. More details about the CRM-HL solutions are available in Ref. [39].

The scale resolving WMLES equations are solved using hpMusic[40] with submission W-047. The WMLES equations are discretized using Flux Reconstruction (FR) or Correction Procedure via Reconstruction (CPR) method and the solution is advanced using an implicit 2nd order optimized BDF scheme with either a LU-SGS or matrix-free GMRES solver. More details about the W-047 submission are available in Ref. [41].

Table 4 High-Order TFG Flow Solution Submissions

Submission	Primary Organization	Flow Solver	Flow Model	Case
A-013	MIT	SANS	RANS-SA	2D CRM-HL(Q1) P1
H-004	MIT	SANS	RANS-SA	2D CRM-HL(Q2) P1-P2
H-005	ORNL, UTK, CREATE-AV	COFFE	RANS-SA	2D CRM-HL(Q2) P1-P2
H-012	ONERA/DAAA	HO_DualMaker(Q2), Nextflow_ITW	URANS-SA	2D CRM-HL(Q1) P2, CRM-HL(Q2) P1-P2
H-023	Boeing	GGNS	RANS-SA	CRM-HL(Q2) P2
H-013	Princeton	maDG	ILES	CRM-HL(Q1) P1-P3
W-047	U Kansas	HpMusic	WMLES	CRM-HL(Q2) P2

VI. 2D CRM-HL Airfoil RANS-SA Verification Case

The 2D CRM-HL airfoil, shown in Fig. 3, was first presented as a challenge test case by the AIAA Meshing, Visualization, and Computational Environments Technical Committee (MVCE-TC) to determine meshing impacts on RANS CFD solutions [42]. Both meshes and grid convergence studies [24, 31, 32, 43–46] from this effort are available on the Turbulence Modeling Resource (TMR) website [47].

The HLPW-4 asked participants to verify their implementation of the SA turbulence model via a code-to-code comparison. The HLPW-4 verification exercise flow conditions are standard sea-level with Mach 0.2, Reynolds number of 5×10^6 based on reference chord (slat and flap stowed), and 16° angle of attack. The farfield is located 1,000 chords away. For this flow condition the asymptotic ($h \to 0$) forces are $C_L \approx 3.803$ and $C_D \approx 0.0605$ (taken from previous rigorous efforts to establish asymptotic values [32, 43]). Three groups submitted 2D CRM-HL verfication results: H-004/A-013, H-005, and H-012.

The lift and drag mesh convergence studies shown in Fig. 4 use Q1 TMR meshes, the Q1 and Q2 meshes generated by H-003, and adapted meshes generated by H-004/A-013 using metric-based mesh adaptation and the Boeing EPIC mesh generator[48] (which can generate Q2 and Q3 meshes in 2D, but not in 3D). Solutions computed by the RANS and ADAPT TFGs are shown in gray for reference (all mesh adapted results are plotted with dash-dot lines). Figs. 4a and 4b show a larger scale on the vertical axis, and Figs. 4c and 4d show the same data with a smaller vertical scale to help distinguish the HO-TFG submissions.

Second order accurate P1 solutions using TMR meshes were submitted by H-005.3 and A-013.1. As shown in

Fig. 4a, while the C_L convergence from the RANS-TFG results appear to be approaching the asymptotic C_L value, they are significantly lower than the H-005.3 and A-013.1 values. The TMR meshes appear to need to be refined two or three more times in order for the RANS-TFG results to each $C_L \approx 3.803$. Similarly, the drag shown in Fig. 4b is over predicted by the RANS-TFG solutions. Since all the discretization schemes from the RANS-TFG and H-005.3/A-013.1 are formally 2$^{\text{nd}}$-order accurate, the primary reason for the difference in the convergence curves is the discretization scheme. All of the RANS-TFG solutions use finite volume/difference schemes whereas the HO-TFG results use finite element discretizations.

While the lift converges from below the asymptotic lift value using the TMR meshes, the lift is converging from above for the submissions H-004.1, H004.2, H-005.1, and H-005.2 using the GridPro meshes. A similar reversal to converging from below is observed in the drag. The H-004.1 and H-005.1 P1 solutions on the coarse GridPro meshes are closer to the asymptotic lift and drag values. However, the finest P1 solution using the GridPro mesh actually has a higher error than those obtained with the finest TMR mesh. The P2 H-004.2 and H-005.2 solutions computed using the GridPro Q2 meshes have a lower lift and drag error relative to the P1 solutions. Both P2 solutions "flatline" after the 2$^{\text{nd}}$ coarsest mesh, and the 2$^{\text{nd}}$ H-005.2 solution agrees well with the asymptotic lift and drag values. However, the H-004.2 solutions have stagnated at lift and drag values that are at a constant offset. While the H-004.2 solutions in the absence of any other data would be considered converged, it is instead a situation where increasing the DOFs is not reducing the numerical error. In other words, the DOFs are primarily added in regions where the numerical error is already low and not added in regions where the numerical error is high. This observation is reinforced by the H-004.3 and A-013.2 solutions computed using output-based mesh adaptation where meshes are generated such that the estimated numerical drag error is minimized for a series of DOF counts. The A-013.2 adapted P1 solutions has a comparable convergence history to the other ADAPT-TFG solutions. However, the H-004.3, which combines high-order P2 and Q3 meshes achieves the asymptotic lift and drag values with only approximately 45k DOF (the finest TMR mesh has 6M DOF).

One last note, the H-012 results are not exhibiting convergence using the GridPro meshes. However, H-012 uses an explicit solver with local time stepping which failed to converge to a steady solution, temporal averaged values are presented here. There is no theoretical guarantee that a temporally averaged solution using local time stepping should converge to the same values as a steady state solution, and it's likely the averaging process was insufficient to observe grid convergence. One of the major finding of the H-012 is the need to implement an implicit solver which can converge to a steady solution.

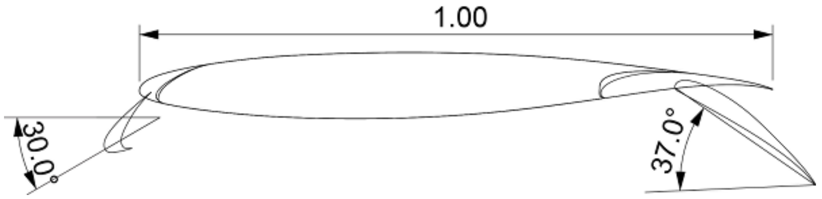

Fig. 3 2D CRM-HL Airfoil Geometry.

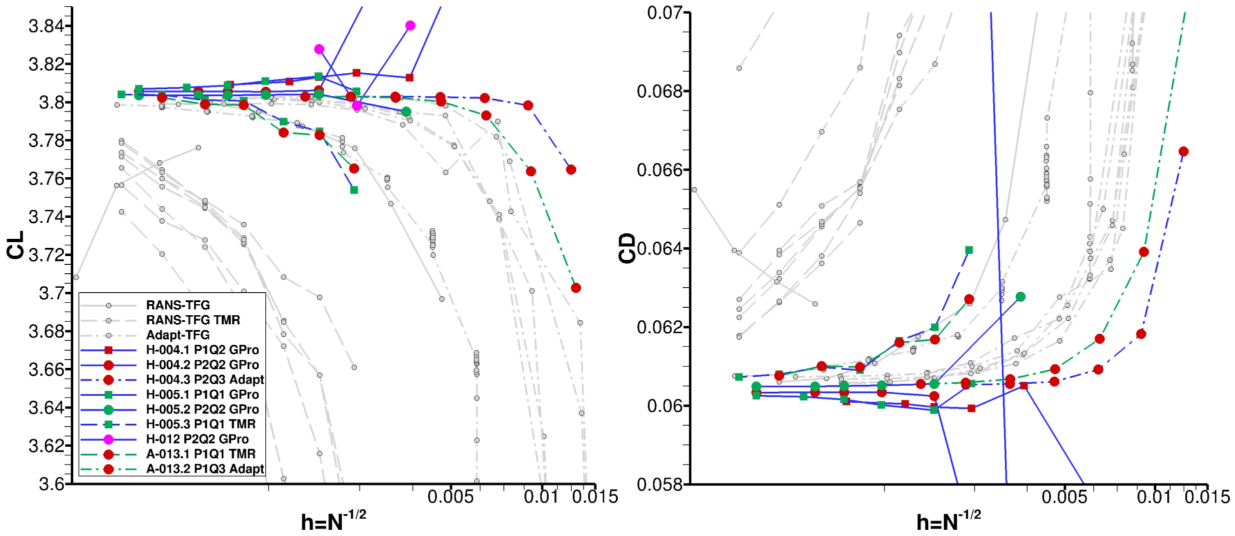

(a) Lift Mesh Convergence (b) Drag Mesh Convergence

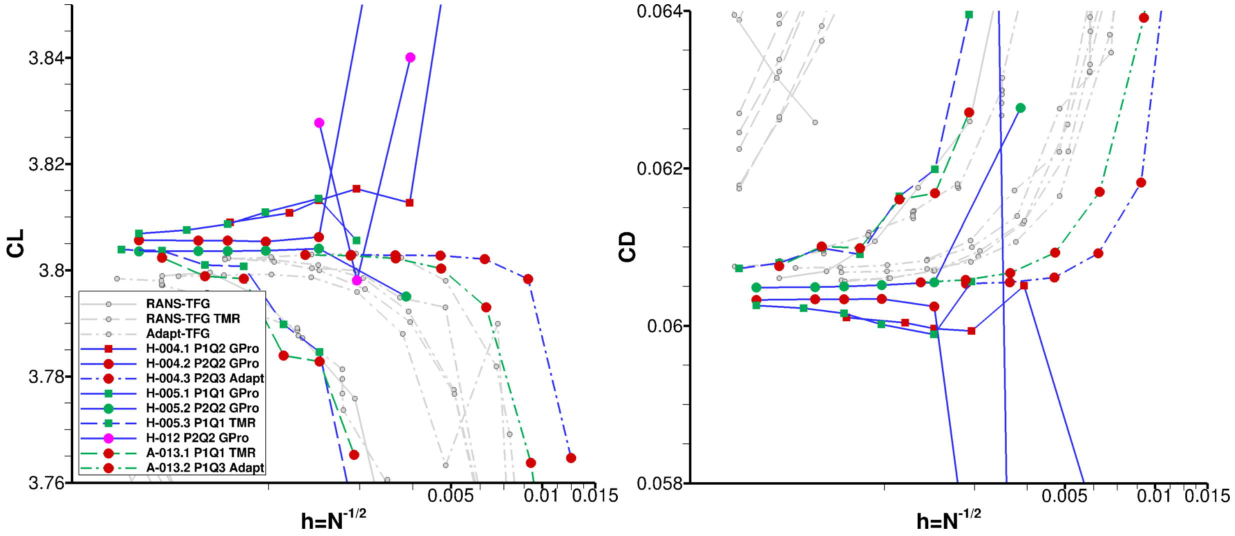

(c) Lift Mesh Convergence Closeup (d) Drag Mesh Convergence Closeup

Fig. 4 2D CRM-HL Airfoil force mesh convergence. Dashed lines are TMR meshes, dash-dot lines are adapted meshes, and solid lines are other meshes.

VII. 3D CRM-HL Degree of Freedom Convergence

Lift and drag convergence with DOF refinement for the 3D CRM-HL configuration at 7.05° angle of attack, Mach 0.2, and Reynolds number 5.49×10^6 based on mean aerodynamic chord, is shown in Fig. 5. The grey lines are best practice results from the RANS, ADAPT, and WMLESLB TFGs for reference.

The ILES results submitted by H-013.1 uses the medium size all-tetrahedra Pointwise® $y^+ \approx 100$ Q1 mesh where the DOF refinement comes from P refinement. The H-013 P1 through P3 solution have 12M, 30M, and 60M DOF respectively. The finest P3 results have a lift value in the range of the reference results from the other TFGs, but the drag values are under predicted. The convergence results of these results are likely limited due to the use of Q1 element with a DG discretization which can significantly degrade the accuracy relative to a Q2 mesh [26, 49]. Further error is introduced by using a lower Reynolds number of 0.5×10^6 to help the stability of the solver.

The WMLES solutions submitted by W-047 used the coarse Pointwise® $y^+ \approx 100$ Q2 mesh with 1M mixed elements. The DOF refinement is achieved with P1 and P2 solutions with 5M and 13M DOF respectively. While the P1 solution under predict the lift, the P2 solution slightly over predicts it relative to the other TFG group results. The drag is consistently over predicted, but could be approaching the value consistent with the other TFGs.

The H-012 results use the coarse and medium Pointwise® meshes with y^+ ranging from ≈ 100 to ≈ 800. The DOF count ranges from 2M to 21M. The “G” notation indicates different DOF locations; 2G has DOF at cell-centers and vertex-centers, 3G adds DOFs at cell-edges, and 4G adds DOFs at cell-faces. The polyhedral mesh representation used by H-012 is shown for two grid levels in Fig. 6. All of the solutions use a quadratic polynomial reconstruction and curved Q2 meshes. A single data point is provided for the H-012 2G formulation. The lift is reasonable for this data point, but the drag is high. The three H-0012 3G data points exhibit lift values in the range consistent with other TFGs, but there is not a clear trend of convergence. The drag values for H-012 3G are again high, and comparable to the 2G data point. The H-012 4G data has similar lift values to the H-012 3G data, but the drag values are significantly over predicted. Some of the issues with DOF convergence may again be related to attempting to compute average values from an explicit scheme with local time stepping.

The last data point was submitted by H-023 using a medium Pointwise® all-tetrahedra Q2 mesh with $y^+ \approx 200$. The RANS-SA P2 solution has approximately 8M DOF. This single data point agrees remarkably well with the other TFG solutions in both lift and drag predictions, particularly given the low DOF count (the finer RANS-TFG solutions have ~500M DOF). Unfortunately, it’s not possible to determine any degree of convergence with only a single data point.

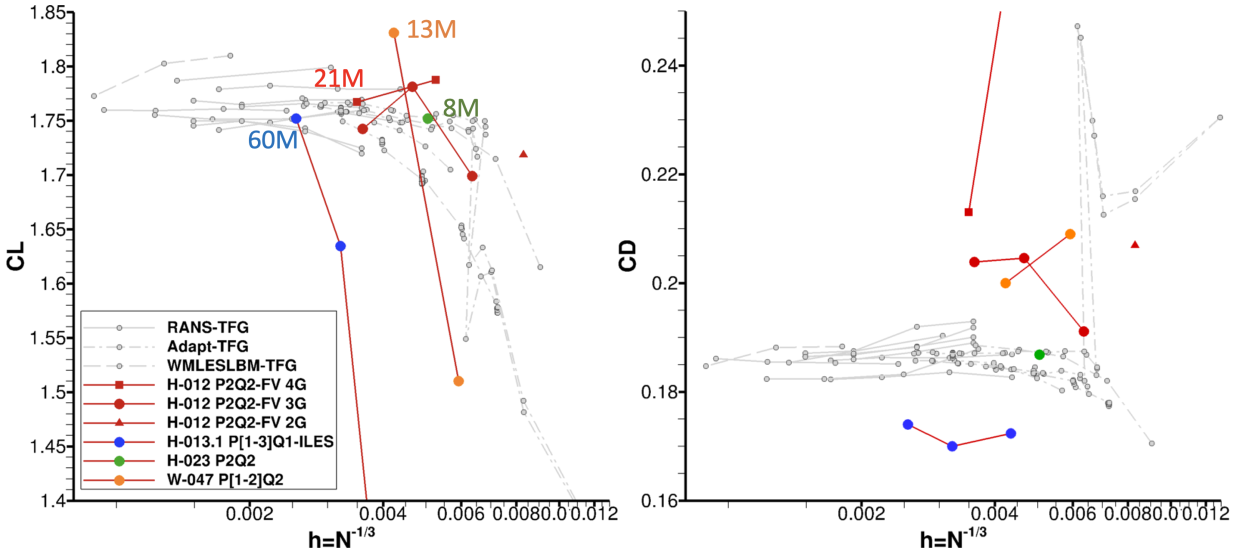

(a)

(b)

Fig. 5 Force convergence for 3D CRM-HL with DOF refinement

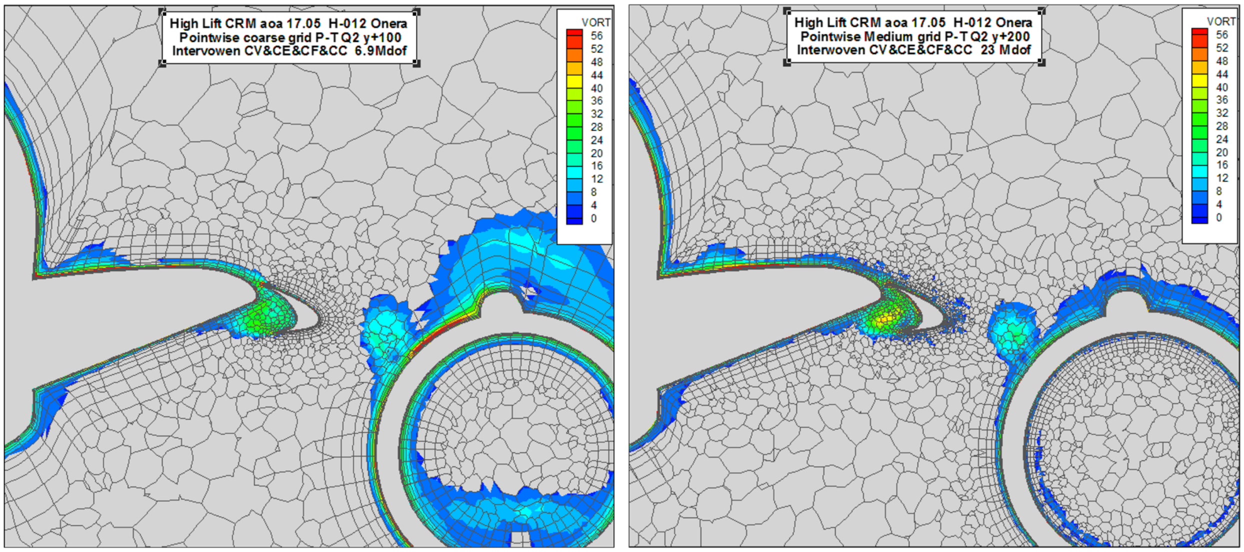

(a)

(b)

Fig. 6 H-0012 3D CRM-HL DOF refinement

VIII. 3D CRM-HL Angle of Attack Sweep

A. RANS-SA

Figure 7 shows the lift curve and drag polar for the H-012 and H-023 RANS-SA submissions. Best practice reference solutions from the RANS and ADAPT TFGs using RANS-SA are also included in grey. The corrected experimental data is also included in this figure. The H-012 solution uses the finest 4G mesh with 21M DOF. The lift values at lower angles of attack are predicted reasonably well. However, while the approximate angle of attack where $C_{L_{max}}$ occurs agrees well with the other TFG data and the experiment, the lift values are under predicted. The drag values are also over estimated for all angles of attack, which is consistent with the over estimation observed in the mesh convergence study. Again, the single data point submitted by H-023 agrees well both with the other TFG results as well as the experimental data, but this does not provide any indication of how well it would predict $C_{L_{max}}$.

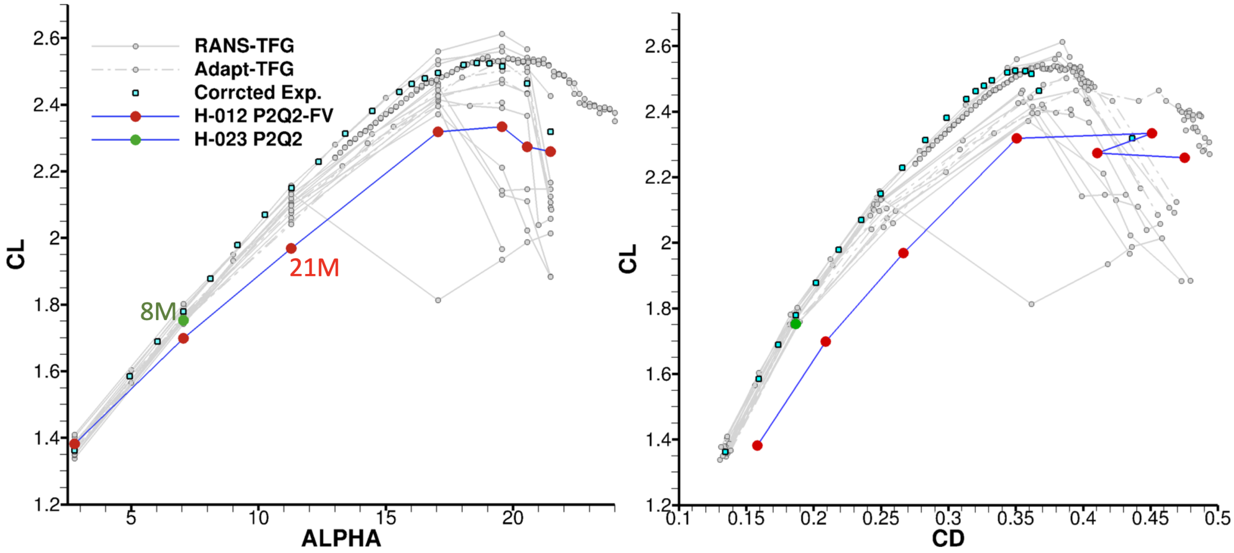

(a) Lift curve

(b) Drag polar

Fig. 7 3D CRM-HL angle of attack sweep using RANS-SA

B. Scale Resolving ILES/WMLES

The lift curve and drag polar computed using ILES by H-013 and WMLES by W-047 is shown in Fig. 8. The H-013 used a P3 discretization with a Q1 mesh, while W-047 used a P2 discretization with the coarse Pointwise® Q2 $y^+ \approx 800$ mesh. The grey lines illustrate the best practice WMLESLB-TFG results for reference. Vorticity contours from two angles of attack solutions, 7.05° and 19.57°, computed by the H-013 and W-047 participants respectively are compared with the coarsest best practice WMLESLB TFG solution, W-020, in Figs. 9 - 12.

Despite using a lower Reynolds number of 0.5×10^6 and only using 60M DOF, the H-013 lift and drag agrees reasonably well with the WMLESLB reference and experimental data at the lower angles of attack. Unfortunately, the lift is significantly under predicted at the higher angles of attack. The 7.05° H-013 and W-020 vorticity fields are shown in Figs 9 and 10. Despite using only one fifth of the DOF count, the P3 H-013 solutions captures many of the same flow features as the W-020 solution. For example, the vortex from the nacelle vortex generator is similar in size and location, as well as the vortices near the root on the upper surface of the wing emanating from the edge of the slat. These features are captured by the P3 H-013 solution despite the visibly significantly coarser mesh as shown in Fig. 9. Note that H-013 mesh is subdivided in order to visualize the P3 polynomials (each tetrahedron is split into 20 sub-elements), and hence is coarser than depicted. Similarities in flow features further downstream on the wing are also observable in Fig. 10.

The W-047 lift curve agrees remarkably well with the WMLESBG-TFG results, in particular when considering it only used 13M DOF. The drag, however, is over predicted at the higher angles of attack. Vorticity contours for the 19.57° W-047 and W-020 solutions are shown in Fig. 11. Again, the W-047 mesh is subdivided in order to visualize the P2 solutions, which artificially increases the apparent mesh resolution. In general, there are more similarities than differences in the solutions despite the order of magnitude difference in DOF. The nacelle vortex generator vortex is captured by the W-047 solution, though the location is slightly closer to the nacelle than what can be observed in the W-047 solution. The vortex on the upper surface near the root of the wing is similar between the two solutions. The vortex below the wing is weaker in the W-047 solution relative to the W-020. The vorticity contours for the two solutions further downstream are shown in Fig. 12. Many of the features are again comparable, though the vortex under the root of the wing is missing, and the vortices in the wake of the nacelle are not as distinct in the W-047 solution. Surface streamlines for the 21.47° W-047 and W-020 solutions are shown in Fig. 13. The separation regions near the root on the upper surface of the wing and on the side of the fuselage are similar in shape and size between the two solutions. The separation regions on the upper surface of the nacelle also agrees reasonably well. However, the "pizza slice" separation regions near the wing tip emanating from the slat brackets are absent in the W-047 solutions. Finally, the W-047 also explored the impact of mesh wall spacing. Figure 14 shows the surface streamlines using the $y^+ \approx 800$ and a mesh with similar resolution but a finer wall spacing of $y^+ \approx 200$. For this case, the finer wall spacing results in separated flow over the entire wing, which is inconsistent with both the experimental data and other CFD solutions from the WMLESLB-TFG. Since the wall model in hpMusic probes the boundary layer at the opposite face of the first element on the wall, the wall model is extracting data from a region with under-resolved turbulence with the finer wall spacing. This could potentially be resolved by using a probe length that is independent of the the size of the first element on the wall, but that type of formulation is more challenging to devise and implement. Hence, wall modeling is still an active area of research.

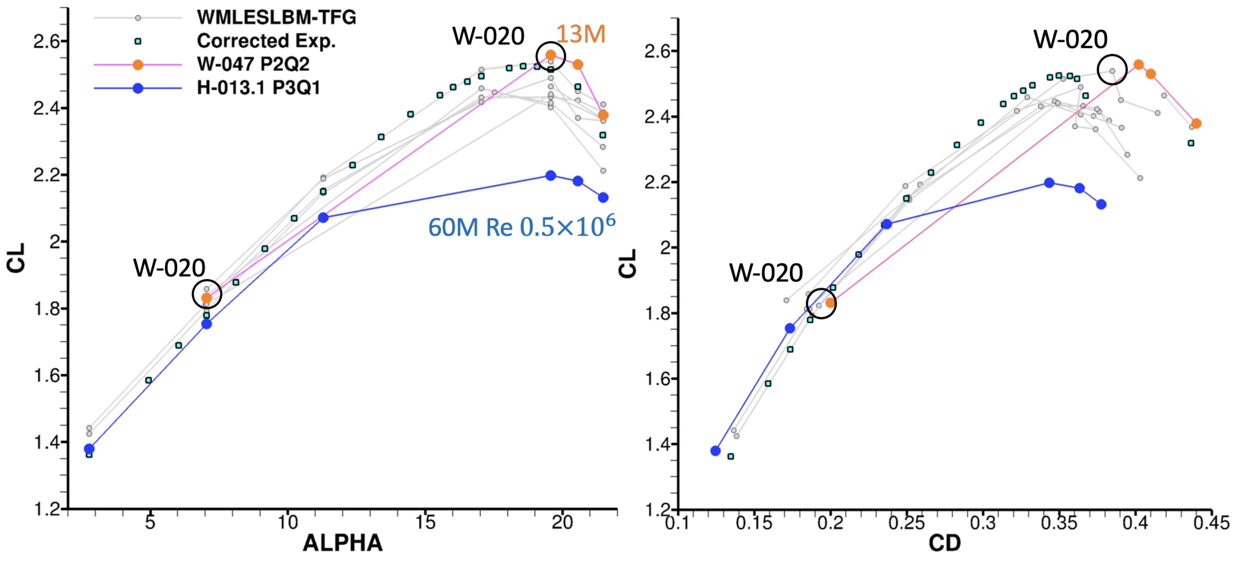

(a) Lift curve

(b) Drag polar

Fig. 8 3D CRM-HL angle of attack sweep using ILES/WMLES

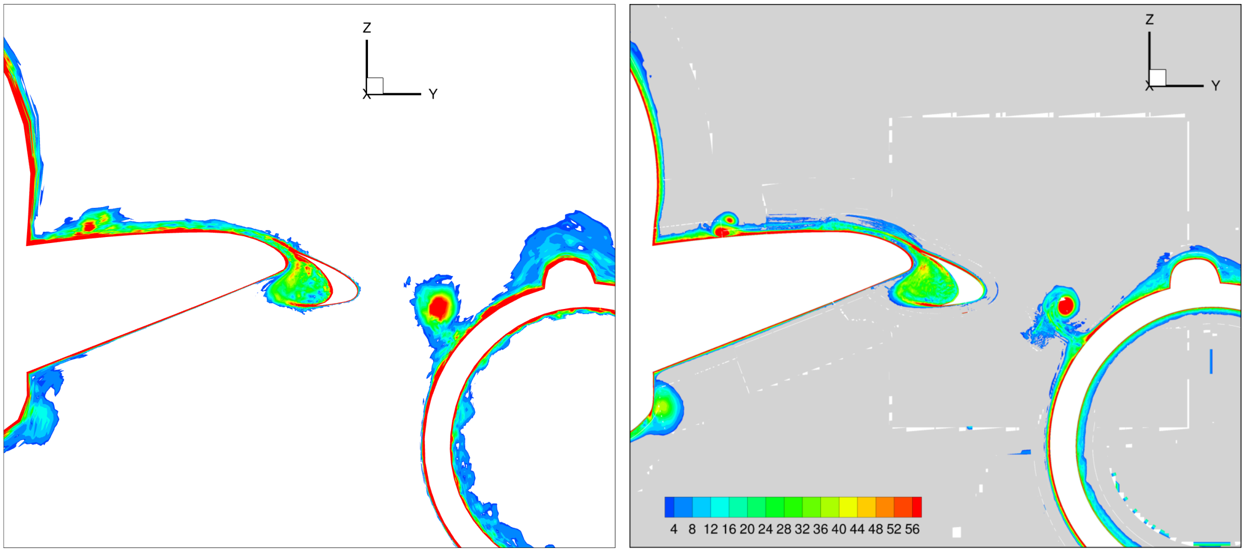

(a) H-013 60M DOF

(b) W-020 360M DOF

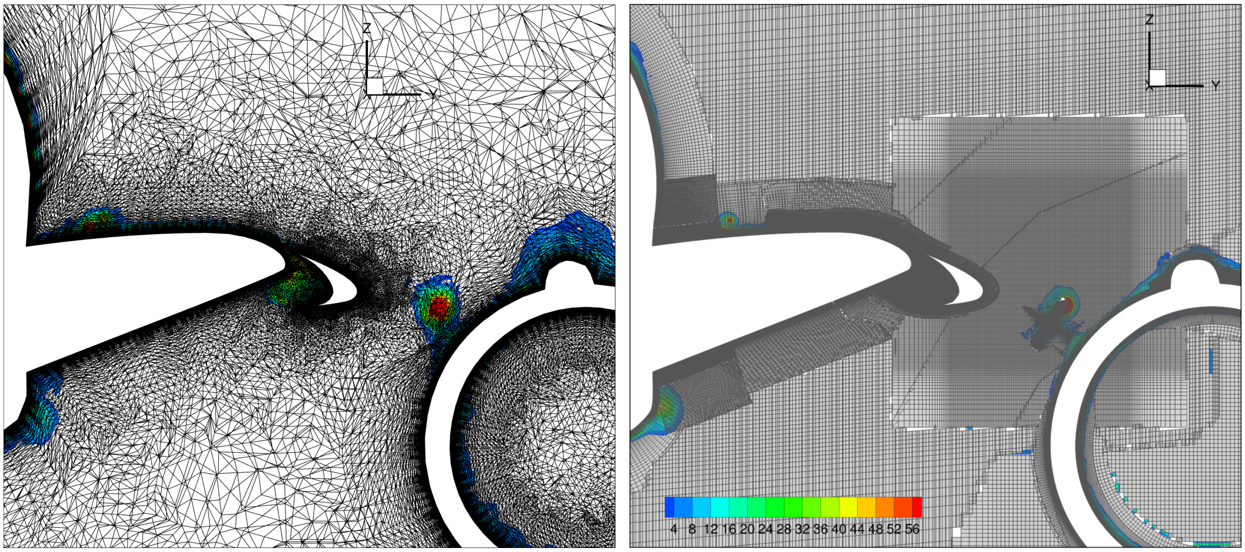

(c) H-013 subdivided mesh

(d) W-020 mesh

Fig. 9 H-013 and W-020 7.05° angle of attack vorticity contours for CFD view 11

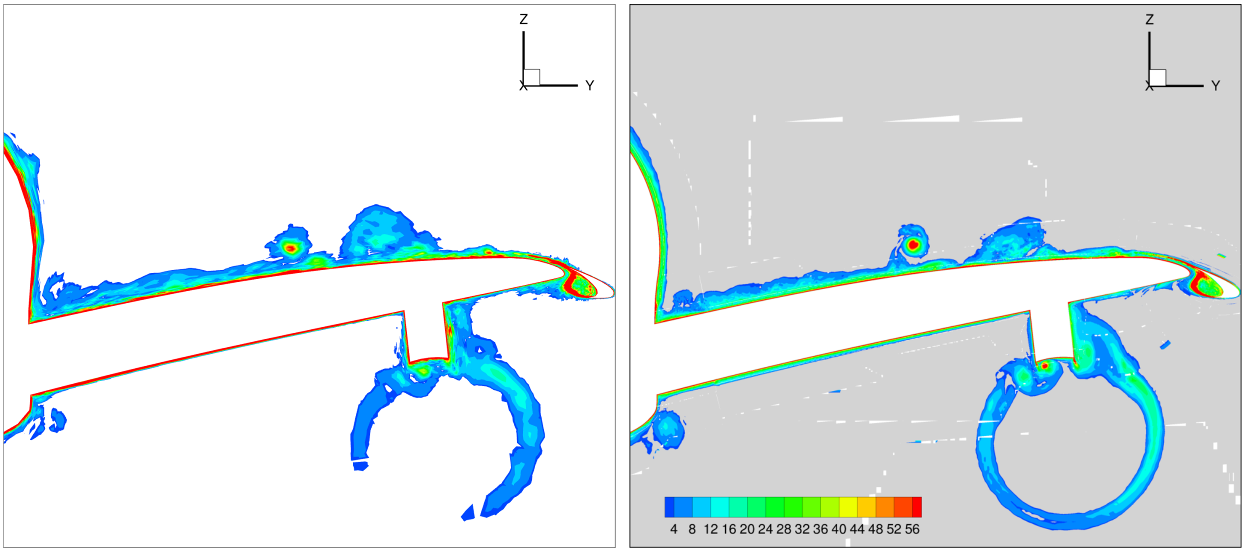

(a) H-013 60M DOF

(b) W-020 360M DOF

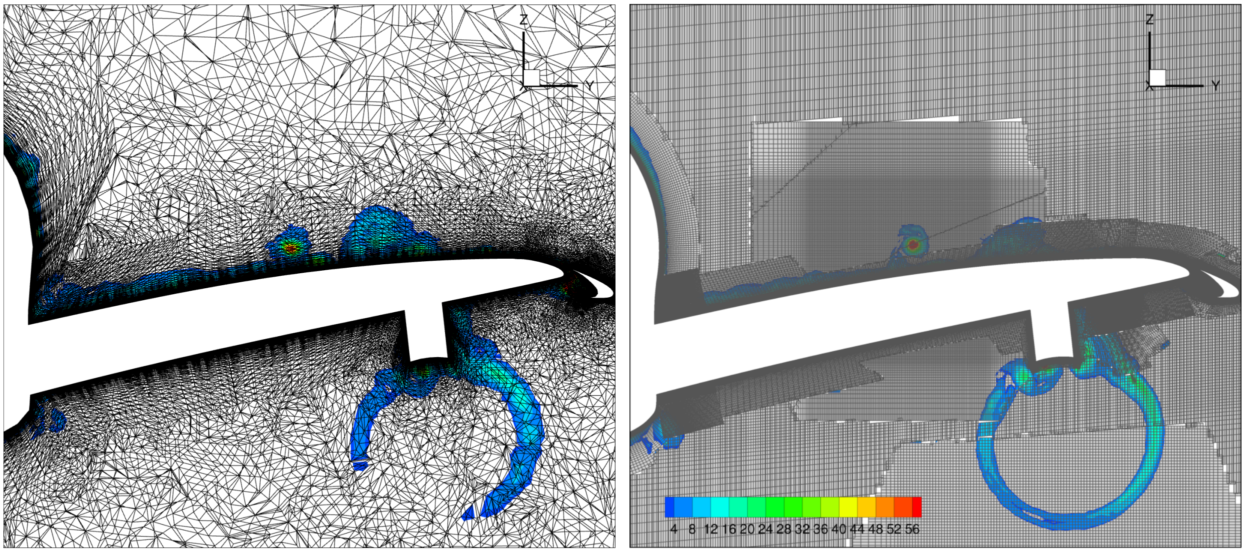

(c) H-013 subdivided mesh

(d) W-020 mesh

Fig. 10 H-013 and W-020 7.05° angle of attack vorticity contours for CFD view 13

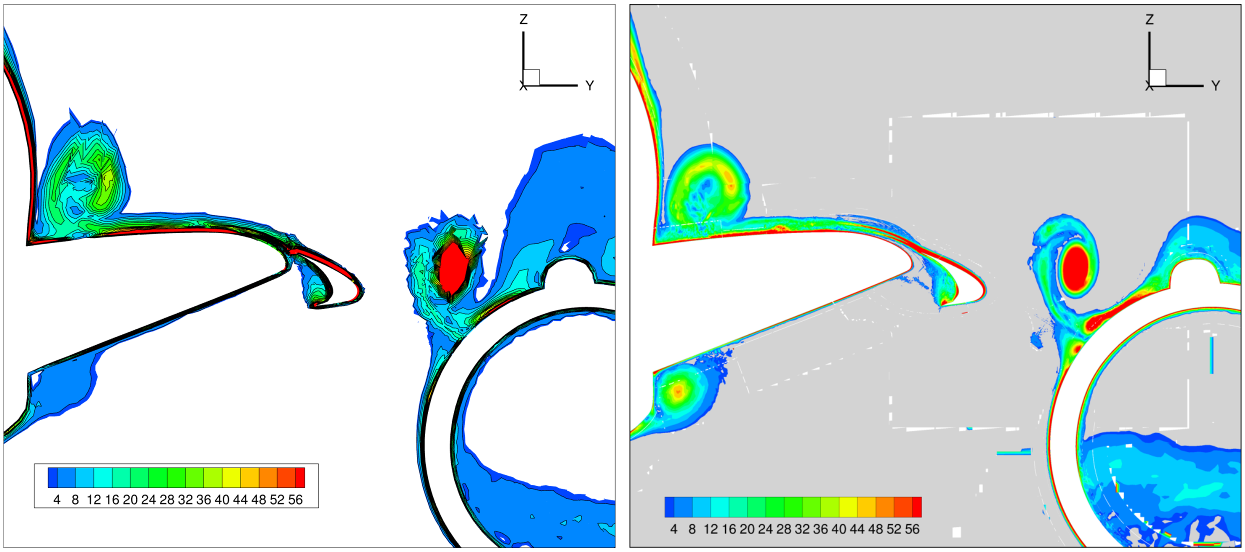

(a) W-047 13M DOF

(b) W-020 360M DOF

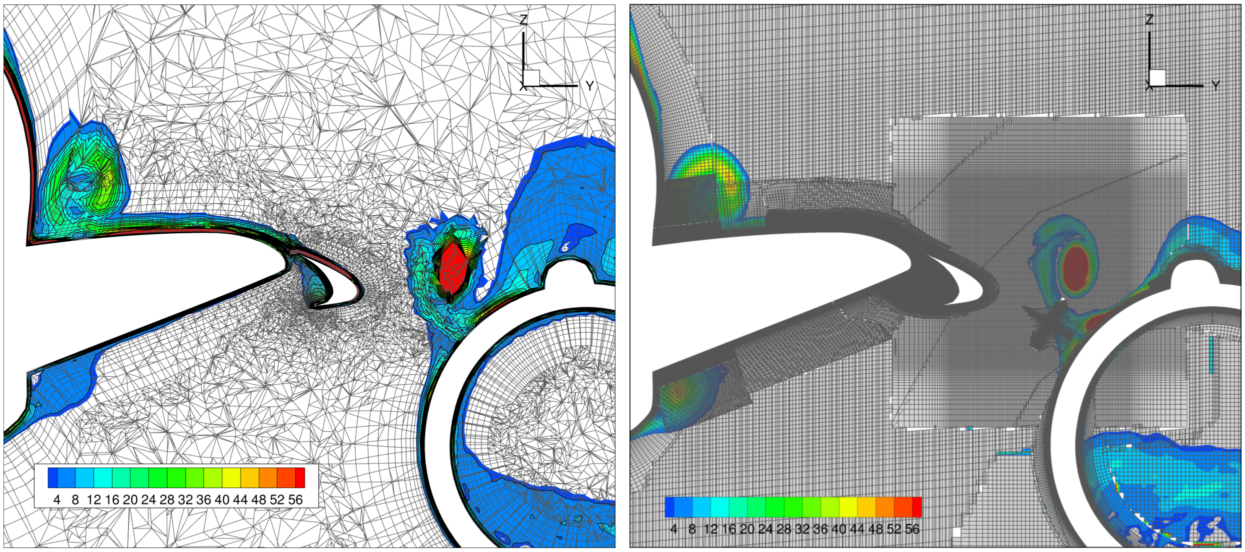

(c) W-047 subdivided mesh

(d) W-020 mesh

Fig. 11 W-047 and W-020 19.57° angle of attack vorticity contours for CFD view 11

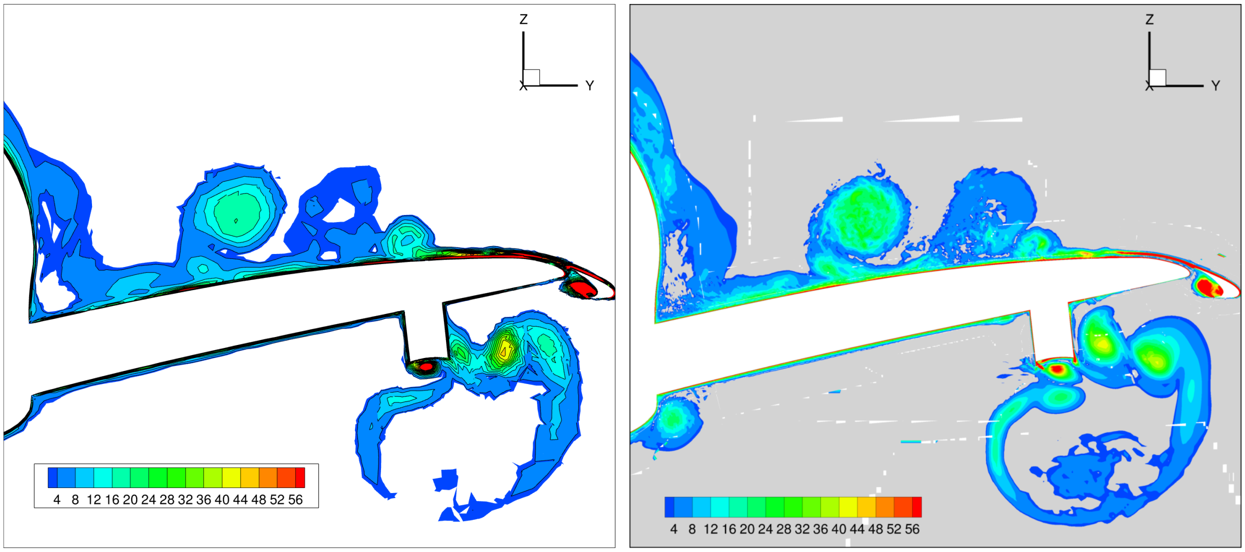

(a) W-047 13M DOF

(b) W-020 360M DOF

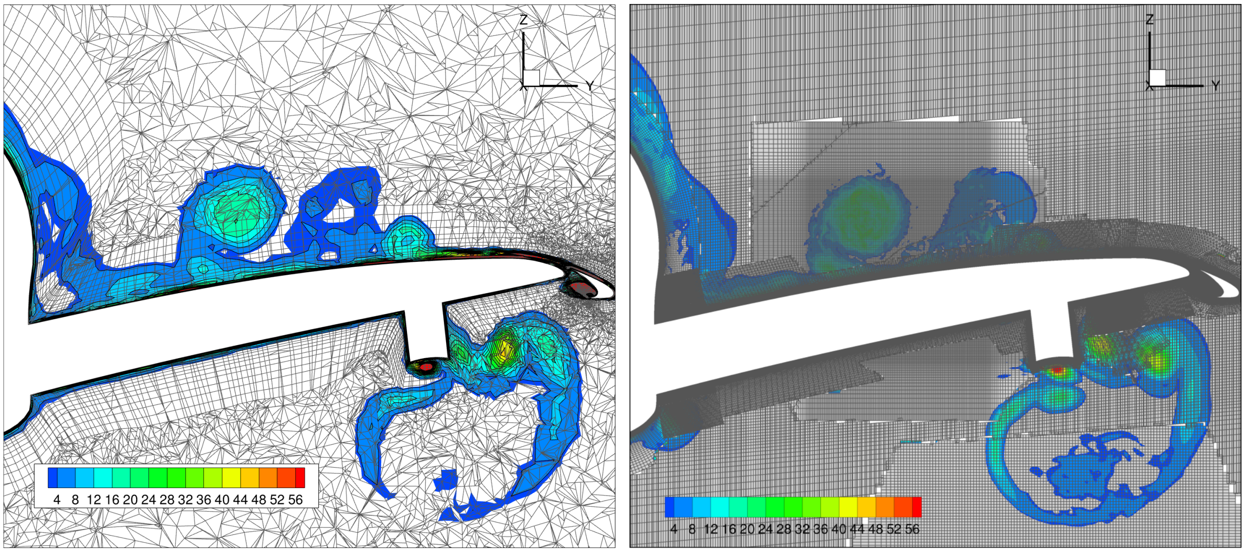

(c) W-047 subdivided mesh

(d) W-020 mesh

Fig. 12 W-047 and W-020 19.57° angle of attack vorticity contours for CFD view 13

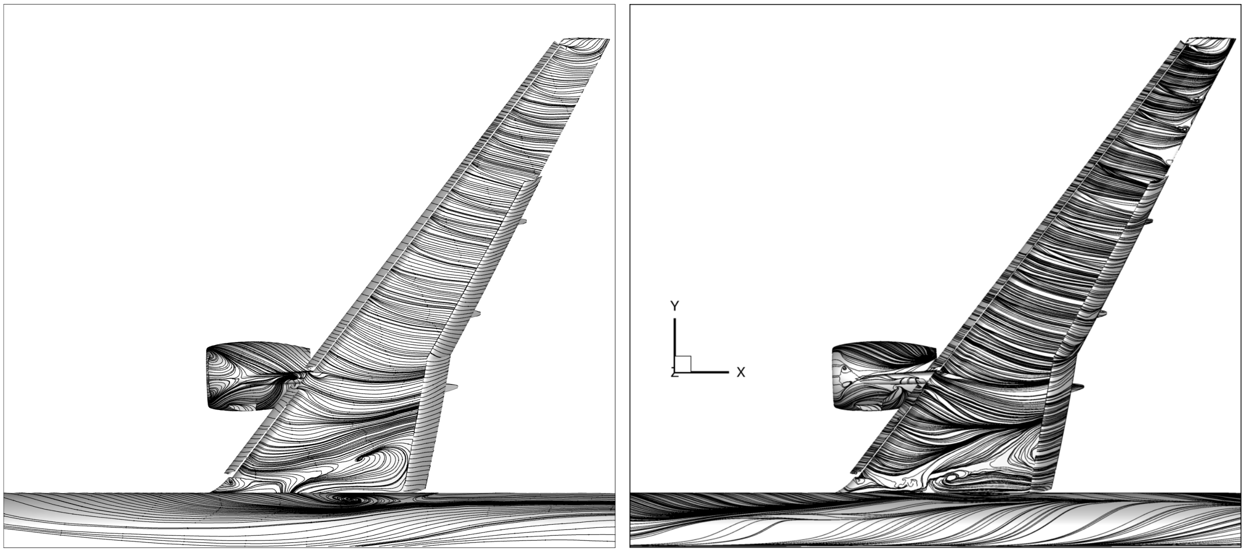

(a) W-047 13M DOF

(b) W-020 360M DOF

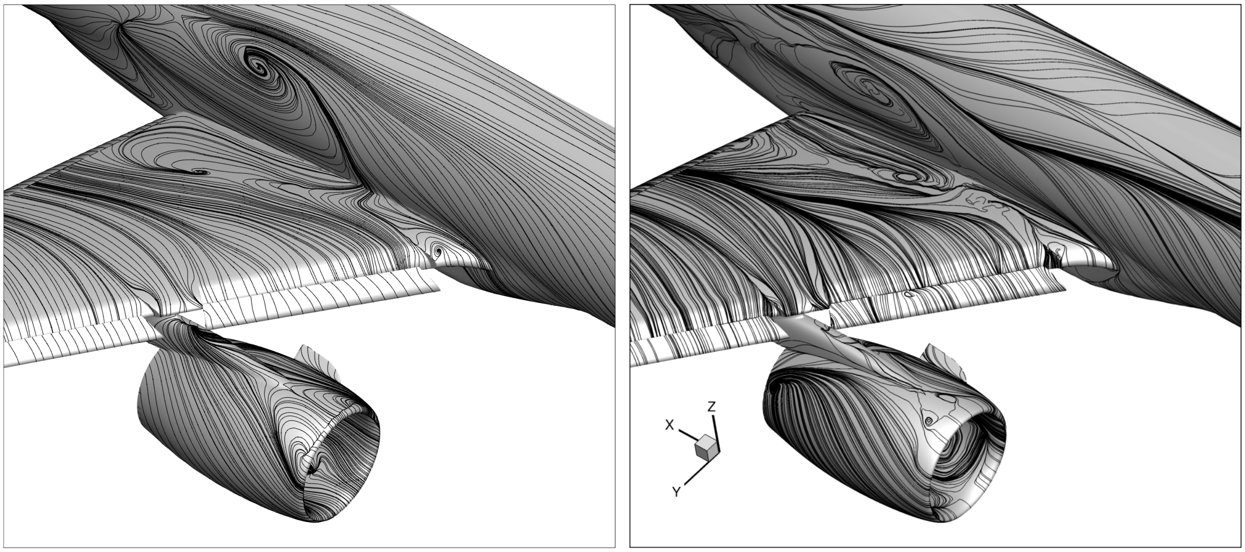

(c) W-047 13M DOF

(d) W-020 360M DOF

Fig. 13 W-047 and W-020 $21.47°$ angle of attack surface streamlines

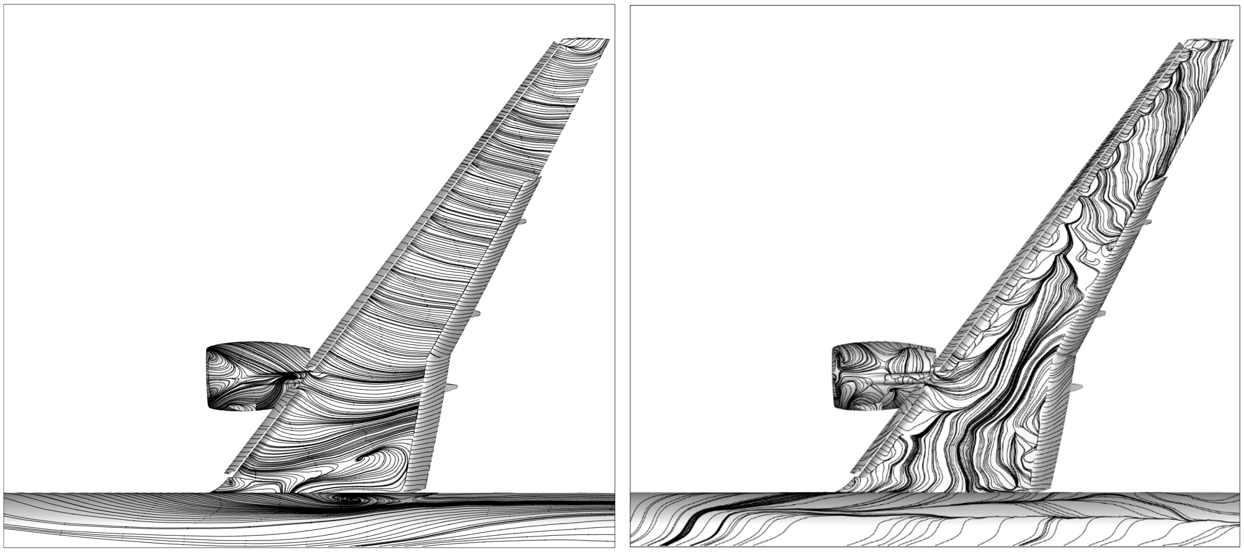

(a) $y^+ \approx 800$ (5mm)   (b) $y^+ \approx 200$ (21mm)

Fig. 14 W-047 $21.47°$ angle of attack surface streamlines

IX. Conclusion

Meshing requirements for high order solutions is subject to the same geometry requirements encountered for linear meshes. Good geometry cleanup will result in less difficulty during mesh generation. This includes the modeling of pinch point regions where the Wing Under Slat Surfaces meets the Wing geometry. But mesh curving operations have to ensure the curved edges do not introduce grid crossing at this locations.

Mesh sizes were critically important for the HO solver participants. Computer resource availability required much coarser linear meshes than the workshop supplied meshes. A coarser mesh sequence consistent with the HLPW-4 meshing guidelines was still too large for most of the HO-TFG solver participants. So, an extremely coarse set of meshes was created as the starting linear meshes. These were small enough that, when elevated to higher order, the mesh sizes were manageable.

The HO-TFG also required meshes with different viscous normal spacing. The traditional $y^+ \approx 1$ meshes were too clustered to enable WMLES computations. So the meshes provided included versions suitable for RANS calculations, with y^+ in the range of 1, and versions where the initial spacing varied for y^+ values ranging from 10 to 800.

The 2D CRM-HL verification case demonstrated the potential for high-order methods to reduce numerical error. For example, FEM solutions computed using the TMR meshes have significantly lower error in lift and drag relative to the finite volume solutions computed on the same meshes. However, this level of improvement is likely both mesh dependent and dependent on the flow features of a particular case. Using P2 solutions with the Q2 GridPro meshes further reduced the error in lift and drag at lower DOF. However, surprisingly, the two P2 submissions with the Q2

GridPro meshes appear to have converged to two slightly different solutions. The cause of this discrepancy is not evident. Finally, the P2 solution combined with output-based mesh adaptation demonstrates the true potential for higher-order methods; the mesh adapted solution achieves similar lift and drag errors with 45k DOF as the solution using the 6M DOF TMR mesh. The major barrier towards applying these methods to 3D configurations is the ability to generate anisotropic adapted curved meshes.

The DOF refinement study for the 3D CRM-HL showed that both the RANS and WMLES/ILES solutions are able to achieve lift values comparable to other TFG solutions, but the drag values are generally over/under-predicted. However, due to limited computational resources, the DOF counts used by the HO participants are significantly coarser relative to the other TFG submissions. The same general trend is observed in the angle of attack sweep for both RANS and scale resolving solutions. Again, all solutions would likely benefit from a larger DOF count. The vorticity contours and surface streamlines demonstrated that the high-order scale resolving methods generally captured many of the same features observed with a finite volume solutions using more than an order of magnitude higher DOF counts. However, the y^+ study revealed that the wall modeling formulation does exhibit mesh sensitivities that warrant further investigation.

In conclusion, the HO-TFG did demonstrate that both high-order curved meshes can be generated and high-order solutions obtained for the CRM-HL, and there is a potential for high-order methods to reduce the DOF count required to obtain accurate solutions.

Acknowledgments

The authors would like to thank all the HO-TFG participants, Nashat Ahmad, Payam Dehpanah, Peter Eiseman, Ryan Glasby, Kevin Holst, Scott Imlay, Dmitry Kamenetskiy, Jean-Marie Le Gouez, Mark Lohry, Adrien Loseille, Behzad Reza Ahrabi, Xevi Roca, Eloi Ruiz-Gironés, and Z. J. Wang, for their insights during the bi-weekly meetings and hard work that contributed to the success of the workshop. The authors are also grateful for all the efforts by the workshop lead organizers, Christopher Rumsey, Jeffrey Slotnick, and Carolyn Woeber, for their vision and dedication towards furthering the capabilities in the CFD community.

This manuscript has been authored, in part, by UT-Battelle, LLC, under contract DE-AC05-00OR22725 with the US Department of Energy (DOE). The U.S. government retains the publisher, by accepting the article for publication, acknowledges that the U.S. government retains a nonexclusive, paid-up, irrevocable, worldwide license to publish or reproduce the published form of this manuscript, or allow others to do so, for U.S. government purposes. DOE will provide public access to these results of federally sponsored research in accordance with the DOE Public Access Plan (https://energy.gov/downloads/doe-public-access-plan).

References

[1] Rumsey, C. L., "The 4th AIAA CFD High Lift Prediction Workshop (HLPW-4)," `https://hiliftpw.larc.nasa.gov`, 2022.

[2] Woeber, C., "3rd AIAA Geometry and Mesh Generation Workshop," `https://www.gmgworkshop.com`, 2022.

[3] Rumsey, C. L., Slotnick, J., Long, M., Stuever, R., and Wayman, T., "Summary of the first AIAA CFD high-lift prediction workshop," *Journal of Aircraft*, Vol. 48, No. 6, 2011, pp. 2068–2079. https://doi.org/10.2514/1.C031447.

[4] Rumsey, C. L., and Slotnick, J. P., "Overview and summary of the second AIAA high-lift prediction workshop," *Journal of Aircraft*, Vol. 52, No. 4, 2015, pp. 1006–1025. https://doi.org/10.2514/1.C032864.

[5] Rumsey, C. L., Slotnick, J. P., and Sclafani, A. J., "Overview and Summary of the Third AIAA High Lift Prediction Workshop," *Journal of Aircraft*, Vol. 56, No. 2, 2019, pp. 621–644. https://doi.org/10.2514/1.C034940.

[6] Chawner, J. R., Michal, T. R., Slotnick, J. P., and Rumsey, C. L., "Summary of the 1^{st} AIAA Geometry and Mesh Generation Workshop (GMGW-1) and Future Plans," AIAA 2018-0128, 2018. https://doi.org/10.2514/6.2018-0128.

[7] Woeber, C., Masters, J. S., and McDaniel, D. R., "Summary of Exascale and Remeshing Efforts for the Second Geometry and Mesh Generation Workshop," AIAA 2019-3458, 2019. https://doi.org/10.2514/6.2019-3458.

[8] Lacy, D. S., and Clark, A. M., "Definition of Initial Landing and Takeoff Reference Configurations for the High Lift Common Research Model (CRM-HL)," AIAA 2020-2771, 2020. https://doi.org/10.2514/6.2020-2771.

[9] Evans, A. N., Lacy, D. S., Smith, I., and Rivers, M. B., "Test Summary of the NASA High-Lift Common Research Model Half-Span at QinetiQ 5-Metre Pressurized Low-Speed Wind Tunnel," AIAA 2020-2770, 2020. https://doi.org/10.2514/6.2020-2770.

[10] Allmaras, S. R., Johnson, F. T., and Spalart, P. R., "Modifications and clarifications for the implementation of the Spalart-Allmaras turbulence model," Seventh International Conference on Computational Fluid Dynamics, Big Island, Hawaii, 2012.

[11] Pita, C. M., and Woeber, C., "HLPW4/GMGW3: Summary of Unstructured Fixed Mesh Generation Efforts for RANS Analyses," AIAA 2022-3209, 2022. https://doi.org/10.2514/6.2022-3209.

[12] Ashton, N., Batten, P., Cary, A. W., Holst, K. R., and Skaperdas, V., "Summary of the 4th High-Lift Prediction Workshop Hybrid RANS/LES Technology Focus Group," *Journal of Aircraft*, 2023. https://doi.org/10.2514/1.C037329.

[13] Kiris, C., Ghate, A., and Browne, O., "HLPW-4/GMGW-3: Wall-Modeled LES and Lattice-Boltzmann Technology Focus Group Workshop Summary," *Journal of Aircraft*, 2023. https://doi.org/10.2514/1.C037193.

[14] Ollivier-Gooch, C. F., and Coder, J. G., "HLPW-4/GMGW-3: Fixed-Grid RANS Technology Focus Group Workshop Summary," *Journal of Aircraft*, 2023. https://doi.org/10.2514/1.C037184.

[15] Park, M., Alauzet, F., and Michal, T., "HLPW-4/GMGW-3: Mesh Adaptation for RANS Technology Focus Group Workshop Summary," *Journal of Aircraft*, 2023. https://doi.org/10.2514/1.C037192.

[16] Rumsey, C. L., Slotnick, J. P., and Woeber, C. D., “HLPW-4/GMGW-3: Overview and Workshop Summary,” *Journal of Aircraft*, 2023. https://doi.org/10.2514/1.C037168.

[17] Giles, M. B., and Süli, E., “Adjoint methods for PDEs: a posteriori error analysis and postprocessing by duality,” *Acta Numerica*, Vol. 11, 2002, pp. 145–236. https://doi.org/10.1017/S096249290200003X.

[18] Houston, P., and Süli, E., “*hp*-adaptive discontinuous Galerkin finite element methods for first-order hyperbolic problems,” *SIAM Journal on Scientific Computing*, Vol. 23, No. 4, 2001, pp. 1226–1252. https://doi.org/10.1137/S1064827500378799.

[19] Karman, S. L., “Mixed-Order Curving for Viscous Meshes,” AIAA 2019-3317, 2019. https://doi.org/10.2514/6.2019-3317.

[20] Ruiz-Gironés, E., and Roca, X., “Imposing boundary conditions to match a CAD virtual geometry for the mesh curving problem,” *International Meshing Roundtable*, Springer, 2018, pp. 343–361. https://doi.org/10.1007/978-3-030-13992-6_19.

[21] Ruiz-Gironés, E., Gargallo-Peiró, A., Sarrate, J., and Roca, X., “Automatically imposing incremental boundary displacements for valid mesh morphing and curving,” *Computer-Aided Design*, Vol. 112, 2019, pp. 47–62. https://doi.org/10.1016/j.cad.2019.01.001.

[22] Ruiz-Gironés, E., and Roca, X., “Automatic Penalty and Degree Continuation for Parallel Pre-Conditioned Mesh Curving on Virtual Geometry,” *Computer-Aided Design*, 2022, p. 103208. https://doi.org/10.1016/j.cad.2022.103208.

[23] Rumsey, C. L., “The 4th AIAA CFD High Lift Prediction Workshop (HLPW-4): Grids,” https://hiliftpw.larc.nasa.gov/Workshop4/grids.html, 2022.

[24] Masters, J. S., Lynch, C. E., and Galsby, R. S., “Kestrel Results on a 2D Cut of the High Lift Common Research Model Wing,” AIAA 2021–0942, 2020. https://doi.org/10.2514/6.2021-0942.

[25] Galbraith, M. C., Allmaras, S. R., and Darmofal, D. L., “A verification driven process for rapid development of CFD software,” AIAA 2015-0818, January 2015. https://doi.org/10.2514/6.2015-0818.

[26] Galbraith, M. C., Allmaras, S. R., and Darmofal, D. L., “SANS RANS solutions for 3D benchmark configurations,” AIAA 2018-1570, January 2018. https://doi.org/10.2514/6.2018-1570.

[27] Huang, A. C., Carson, H. A., Allmaras, S. R., Galbraith, M. C., Darmofal, D. L., and Kamenetskiy, D. S., “A Variational Multiscale Method with Discontinuous Subscales for Output-Based Adaptation of Aerodynamic Flows,” AIAA 2020–1563, January 2020. https://doi.org/10.2514/6.2020-1563.

[28] Huang, A. C., “An Adaptive Variational Mutltiscale Method with Discontinuous Subscales for Aerodynamics Flows,” PhD thesis, Massachusetts Institute of Technology, Department of Aeronautics and Astronautics, November 2019.

[29] Carson, H. A., Huang, A. C., Galbraith, M. C., Allmaras, S. R., and Darmofal, D. L., “Mesh optimization via error sampling and synthesis: An update,” AIAA 2020–0087, January 2020. https://doi.org/10.2514/6.2020-0087.

[30] Carson, H. A., "Provably Convergent Anisotropic Output-Based Adaptation for Continuous Finite Element Discretizations," PhD thesis, Massachusetts Institute of Technology, Department of Aeronautics and Astronautics, Feb. 2019.

[31] Ursachi, C.-I., Galbraith, M. C., Allmaras, S. R., and Darmofal, D. L., "Output-Based Adaptive Reynolds-Averaged Navier–Stokes Higher-Order Finite Element Solutions on a Multielement Airfoil," *AIAA Journal*, Vol. 59, No. 7, 2021, pp. 2532–2545. https://doi.org/10.2514/1.J059968.

[32] Galbraith, M. C., Ursachi, C.-I., Chandel, D., Allmaras, S. R., Darmofal, D. L., Glasby, R. S., Stefanski, D. L., Taylor Erwin, K. R., J. a nd Holst, Hereth, E. A., Mukhopadhaya, J., and Alonso, J. J., "Comparing Multi-Element Airfoil Flow Solutions Using Multiple Solvers with Output-Based Adapted Meshes," *AIAA Journal*, Vol. 60, No. 4, 2022, pp. 2629–2643. https://doi.org/10.2514/1.J060861.

[33] Glasby, R. S., and Erwin, J. T., "Introduction to COFFE: The next-generation HPCMP CREATE^{TM}-AV CFD solver," AIAA 2016-0567, 2016. https://doi.org/10.2514/6.2016-0567.

[34] Le Gouez, J.-M., "High-Order Finite Volume Method for Gas Dynamics on geometrically HO multi-element unstructured grids," AIAA 2020-1788, 2020. https://doi.org/10.2514/6.2020-1788.

[35] Le Gouez, J.-M., "Coupled Solution of 3D Unstructured Finite Volume Discretizations of the RANS Equations on Q2 Primal and Dual Grids. Application to the Test Cases 1b and 2a." AIAA 3808, 2022. https://doi.org/10.2514/6.2022-3808.

[36] Kamenetskiy, D. S., Bussoletti, J. E., Hilmes, C. L., Venkatakrishnan, V., and Wigton, L. B., "Numerical Evidence of Multiple Solutions for the Reynolds-Averaged Navier-Stokes Equations," *AIAA Journal*, Vol. 52, No. 8, 2014, pp. 1686–1698. https://doi.org/10.2514/1.J052676.

[37] Kamenetskiy, D. S., Krakos, J. A., Michal, T. R., Clerici, F., Alauzet, F., Loseille, A., Park, M. A., Wood, S. L., Balan, A., and Galbraith, M. C., "Anisotropic Goal-Based Mesh Adaptation Metric Clarification and Development," AIAA 2022-1245, 2022. https://doi.org/10.2514/6.2022-1245.

[38] Lohry, M. W., and Martinelli, L., "On the development, verification, and validation of a discontinuous Galerkin solver for the Navier-Stokes equations," *Computers & Fluids*, Vol. 223, 2021, p. 104921. https://doi.org/10.1016/j.compfluid.2021.104921.

[39] Lohry, M. W., and Martinelli, L., "Discontinuous Galerkin Implicit Large Eddy Simulation of Tandem Spheres and the High-Lift Common Research Model," AIAA 2022-1375, 2022. https://doi.org/10.2514/6.2022-1375.

[40] Wang, Z., Li, Y., Jia, F., Laskowski, G., Kopriva, J., Paliath, U., and Bhaskaran, R., "Towards industrial large eddy simulation using the FR/CPR method," *Computers and Fluids*, Vol. 156, 2017, pp. 579–589. https://doi.org/10.1016/j.compfluid.2017.04.026.

[41] Wang, Z., "Wall-Modeled Large Eddy Simulation of the NASA CRM High-Lift Configuration with the High-Order FR/CPR Method," AIAA 3395, 2022. https://doi.org/10.2514/6.2022-3395.

[42] Clark, A., Dannenhoffer, J., Gammon, M., Jones, B., Masters, J., Michal, T., Ollivier-Gooch, C., Rodrigo, F., Taylor, N., Thornburg, H., and Woeber, C., "Mesh Effects for CFD Solutions," http://www.gmgworkshop.com/gmgw25.shtml, 2020.

[43] Michal, T., Krakos, J., Kamenetskiy, D., Galbraith, M., Ursachi, C.-I., Park, M. A., Anderson, W. K., Alauzet, F., and Loseille, A., “Comparing Unstructured Adaptive Mesh Solutions for the High Lift Common Research Airfoil,” *AIAA Journal*, Vol. 59, No. 9, 2021, pp. 3566–3584. https://doi.org/10.2514/1.J060088.

[44] Moss, B. R., Bagheri, A. K., and Ronch, A. D., “Effect of Mesh Characteristics on the Flow Solutions around a Multi–element Airfoil using SU2,” AIAA 2020-3218, 2020. https://doi.org/10.2514/6.2020-3218.

[45] Chuen, A. M., and Chan, W. M., “Mesh Effects on Flow Solutions for a 2-D Multi-Element Airfoil Using Structured Overset Methods,” AIAA 2020-3222, 2020. https://doi.org/10.2514/6.2020-3222.

[46] de Souza, R. F., Ferrari, M., and Ferrari, D., “Mesh Effects for 2-D CFD Solutions on a High Lift CRM Wing Section,” AIAA 2021-1361, 2021. https://doi.org/10.2514/6.2021-1361.

[47] “Turbulence Modeling Resource Website,” https://turbmodels.larc.nasa.gov/index.html, 2020.

[48] Michal, T., and Krakos, J., “Anisotropic mesh adaptation through edge primitive operations,” AIAA 2012–159, January 2012. https://doi.org/10.2514/6.2012-159.

[49] Bassi, F., and Rebay, S., “High-Order Accurate Discontinuous Finite Element Solution of the 2D Euler Equations,” *Journal of Computational Physics*, Vol. 138, No. 2, 1997, pp. 251–285. https://doi.org/10.1006/jcph.1997.5454.